Scale resolving simulation of wing lower surface buffet effects induced by the installation of a UHBR nacelle

Spinner, Sebastian* and Rudnik, Ralf†
German Aerospace Center (DLR), Lilienthalplatz 7, 38108 Braunschweig, Germany

Herr, Marius‡ and Probst, Axel§
German Aerospace Center (DLR), Bunsenstrasse 10, 37073 Goettingen, Germany

Radespiel, Rolf¶
Technical University Braunschweig, Hermann-Blenk-Str. 37, 38108 Braunschweig, Germany

The integration of large engine nacelles below the wing of an aircraft is accompanied by a variety of aerodynamic effects such as unsteady shock buffet occurring on the lower surface of the wing. In this study these effects are investigated by applying a hybrid RANS-LES method on a commercial transport aircraft configuration at high subsonic Mach number and low angle of attack. A local region on the wing lower surface confined by the pylon and the fuselage is thereby simulated using an IDDES approach allowing a detailed assessment of the interaction of the transonic shock with the turbulent boundary layer while the remaining computational domain is simulated using a RANS method with a Reynolds-stress turbulence model. To allow a smooth transition between the RANS and the LES region a synthetic turbulence generator is located upstream of the shock which translates the modeled turbulence of the RANS model coming from upstream into local temporal and spatial resolved fluctuations.

Here we show that the IDDES approach accurately computes the wing lower surface buffet effects. Comparisons with wind tunnel experiments show excellent agreement in terms of local pressure distributions and pressure fluctuations on the wing lower surface around the shock and a significant improvement of the simulation accuracy compared to conventional approaches based on pure RANS modeling. Spectral analysis of the unsteady shock motion shows a good agreement between the IDDES and experimental data supporting previous findings that the lower wing buffet phenomenon is associated with Strouhal numbers in the range of 0.2 to 0.4. This Strouhal number range matches with studies on classical buffet on the wing suction side indicating that a similar mechanism is at work.

*Research Scientist, Institute of Aerodynamics and Flow Technologies, Transport Aircraft Division
†Head of Department, Institute of Aerodynamics and Flow Technologies, Transport Aircraft Division
‡Research Scientist, Institute of Aerodynamics and Flow Technologies, C²A²S²E
§Team Lead, Institute of Aerodynamics and Flow Technologies, C²A²S²E
¶Professor (retired), Institute of Fluid Mechanics

Nomenclature

Symbols

α	=	angle of attack, [°]
α_g	=	geometric function in WMLES blending, [-]
c	=	local chord, [m]
C_{DES}	=	calibration constant in LES length scale, [-]
$C_{f,x}$	=	skin friction coefficient along x-axis, [-]
C_p	=	pressure coefficient, [-]
CTU	=	convective time unit, [s]
$\overline{C_p}$	=	time mean of C_p, [-]
δ	=	boundary layer thickness, [m]
δ_{STG}	=	boundary layer thickness at STG, [m]
δ_w	=	wall distance, [m]
Δx	=	local cell length in x-direction, [m]
Δy	=	local cell length in y-direction, [m]
Δz	=	local cell length in z-direction, [m]
Δ_{IDDES}	=	Filter width of IDDES, [m]
f	=	frequency, [1/s]
f_B	=	WMLES blending function, [-]
$\tilde{f_d}$	=	main blending function of IDDES, [-]
f_{dt}	=	IDDES delaying function, [-]
f_e	=	IDDES elevating function, [-]
h_{max}	=	maximum local edge length, [-]
k_{res}	=	resolved turbulent kinetic energy, [m²/s²]
k_{tot}	=	total turbulent kinetic energy, [m²/s²]
l_{hyb}	=	hybrid length scale, [m]
l_{LES}	=	LES length scale, [m]
l_{RANS}	=	RANS length scale, [m]
l_{ref}	=	reference length, [m]
M	=	Mach number, [-]
$\overline{M}$	=	time mean of M, [-]
MAC	=	mean aerodynamic chord, [m]
Re	=	Reynolds number, [-]
σ_{C_p}	=	standard deviation of C_p, [-]
s	=	wing half span, [m]
St	=	Strouhal number, [-]
U_∞	=	freestream velocity, [m/s]
x	=	x-coordinate, [m]
y	=	y-coordinate, [m]
y^+	=	non dimensional wall distance, [-]

Abbreviations

AZDES	=	Automated Zonal Detached Eddy Simulation
CRM	=	Common Research Model
DES	=	Detached Eddy Simulation
DDES	=	Delayed Detached Eddy Simulation
DFG	=	Deutsche Forschungsgemeinschaft
DLR	=	Deutsches Zentrum für Luft und Raumfahrt
ETW	=	European Transonic Wind Tunnel
EWMLES	=	Embedded Wall Modeled Large Eddy Simulation
HGF	=	Helmholtz Gemeinschaft Deutscher Forschungszentren
IDDES	=	Improved Delayed Detached Eddy Simulation
LES	=	Large Eddy Simulation
NASA	=	National Aeronautics and Space Administration
PIV	=	Particle Image Velocimetry
PSD	=	Power Spectral Density
PSP	=	Pressure Sensitive Paint
PT	=	Pressure Tap
RANS	=	Reynolds Averaged Navier Stokes
RSM	=	Reynolds Stress Model
SBLI	=	Shock Boundary Layer Interaction
STG	=	Synthetic Turbulence Generator
uPSP	=	Unsteady Pressure Sensititve Paint
UHBR	=	Ultra High Bypass Ratio
UV	=	Ultra Violet
WMLES	=	Wall Modeled Large Eddy Simulation

I. Introduction

The increase in fan size of turbofan engines has been one of the most prominent developments in commercial transport aircraft of the last few decades. Increasing the size and thereby the bypass ratio is an important factor to push the efficiency of these engines further and thereby reducing fuel consumption and emissions. The current generation of airliners is powered by engines with bypass ratios up to 10 and future designs are expected to use even larger ultra high bypass ratio (UHBR) engines with bypass ratios of around 15.

The main aerodynamic engine integration effects for large engines in classical under-wing-configuration where already identified in early studies using wind tunnel experiments and numerical simulations solving the Euler equations showing that the integration of a large engine to the wing results in an upstream shock movement on the wing suction side and the introduction of additional areas of flow acceleration on the wing pressure side terminated by transonic shocks [1]. Later studies supported these findings and showed that these interference effects became more pronounced for larger nacelles and closer coupling of engine and airframe [2]. When other relevant engine integration factors are taken into account in addition to aerodynamic performance, such as increasing the length of the landing gear to ensure sufficient ground clearance, it was found that at a certain point, the increase in propulsive performance resulting from an increase in BPR is offset by detrimental secondary effects, e.g. due to significant increase in overall aircraft weight [3]. It is therefore important to closely couple the engine and airframe without detrimental aerodynamic interference effects offsetting the efficiency gains. For this reason, many studies focused on the optimum positioning of UHBR engines on the wing [4–6]. For a comprehensive review of recent advances in the topic of UHBR engine integration the reader is referred to [7].

While the above mentioned studies were focused on adequate performance at or around cruise conditions, the high-speed off-design behavior of closely coupled UHBR engines is an area that has received little attention to date. It was found that at high subsonic cruise Mach number, unsteady shock boundary layer interaction (SBLI) can occur on the wing lower surface, pylon, and the nacelle itself. These effects are related to local flow accelerations caused by aerodynamic interference between the large engine body and the wing. These unsteady phenomena are similar to classical buffet effects on the wing upper surface and are relevant for safety and certification and must therefore be taken into account during the design of aircraft. A more detailed understanding of these effects will allow future aircraft to be designed more efficiently and thus contribute to more sustainable aviation.

The numerical simulation of classical transonic shock buffet on complex transport aircraft is a challenging tasks. An unsteady RANS method together with a Reynolds stress turbulence model to simulate classical shock buffet on the NASA Common Research Model (CRM) geometry was applied in [8] showing good quantitative agreement with mean experimental data. In another study Delayed Detached Eddy Simulation (DDES) and Automated Zonal Detached Eddy Simulation (AZDES) as well as unsteady RANS simulations were run to investigate buffet on the NASA CRM [9]. In this study it was found that the application of a Reynolds stress turbulence model resulted in a steady shock, while the Spalart-Allmaras (SA) turbulence model with the quadratic constitutive relation extension gave good agreement for both unsteady RANS and AZDES concerning unsteady characteristics of the shock oscillation on the wing. Another zonal DES approach together with the SA turbulence model was applied by [10] to simulate buffet on the NASA CRM yielding a discrepancy in shock position but showing unsteady effects associated with 3D buffet. Sartor et al. [11] also successfully applied a DDES approach together with the SA turbulence model to simulation transonic shock buffet on the wing of a generic wing-body configuration. While some of these studies where successful in simulating unsteady shock buffet phenomena using RANS based approaches, the prediction capabilities of RANS methods in this field are limited and often case dependent. Therefore more sophisticated LES based simulations as mentioned above are used to study the phenomenon in more detail.

In 2020 the DFG (Deutsche Forschungsgemeinschaft, German Research Foundation) established the research initiative FOR 2895 entitled "Unsteady flow and interaction phenomena at High-Speed Stall conditions" to address high speed buffet phenomena and associated engine integration effects as well as wing-tail interaction effects [12]. The project is aimed at applying hybrid RANS-LES methods to investigate these phenomena with a high level of fidelity and provides the framework for the present study.

In order to validate the hybrid methods, dedicated wind tunnel experiments funded by the HGF (Helmholtz-Gemeinschaft Deutscher Forschungszentren, Helmholtz Association) were conducted in the ETW (European Transonic Wind Tunnel) facility[13]. For this purpose, the XRF-1 wind tunnel model [14] was provided by Airbus and was equipped with two instrumented UHBR through flow nacelles designed and integrated by DLR [15] as well as a new instrumented HTP. A unique aspect of these test campaigns was the extensive application of unsteady pressure sensitive paint (PSP) [16] and particle image velocimetry (PIV) [17] measurements to investigate buffet phenomena at flight relevant Reynolds numbers under cryogenic conditions.

A detailed analysis of lower wing buffet effects induced by the installation of a UHBR nacelle was performed based on unsteady PSP measurements from the aforementioned wind tunnel tests[18]. It was found that unsteady SBLI occurs at low angles of attack and high subsonic Mach number due to the formation of a half open channel between the nacelle, pylon, wing lower surface and fuselage. Displacement effects in this half open channel result in a transonic shock that interacts with the viscous boundary layer and results in an unsteady shock induced separation. The analysis showed that the phenomenon is present over the entire range of Reynolds numbers investigated ranging from 3.3 million up to 25 million. Spectral analysis indicated that the unsteady shock motion behaves similarly to the buffet on the wing upper surface at high angles of attack.

Complementary to the experimental investigations, an advanced hybrid RANS-LES approach based on Reynolds-stress modeling in the RANS regions and synthetic-turbulence injection at the interface to LES was developed within FOR 2895 [19], [20]. During conception of the study this was deemed a requirement as the flow in the wing pylon area, especially in the intersection regions, is of highly anisotropic nature and therefore Reynolds stress models (RSM), which allow to account for turbulent anisotropy, are expected to give superior results over eddy viscosity based models. In this study, the newly developed RSM based approach is applied with the DLR flow solver TAU to locally resolve the interaction of the transonic shock with the turbulent boundary using LES while the surrounding flow around the remaining aircraft is modeled by a RANS approach.

II. Setup

The test case was based on a previous study investigating the lower wing buffet phenomenon using experimental data [18]. An overview of the flow conditions is given in Table 1. The Reynolds number of 3.3 million was selected to allow an adequate spatial resolution of the complex scale resolving simulations while limiting the total number of grid points and in addition keeping a link to the wind tunnel experiments extending from Reynolds number of 3.3 million up to flight relevant Reynolds numbers of 25 million.

Note that the chosen angle of attack for this study is unexpectedly low. These very low angles of attack at high cruise Mach number pose a limit to the flight envelope and are relevant for design speed specifications provided by the Federal Aviation Administration [21]. For example, when demonstrating V_{DF} (Demonstrated Flight Diving Speed) the aircraft has to fly at a flight path of -7.5° before performing a pull up maneuver. Knowledge on the aerodynamic behavior of the aircraft and the buffet phenomena that may occur at these conditions is therefore essential.

Table 1 Investigated flow conditions.

M [-]	Re [-][1]	α [°]
0.84	3.3×10^6	-4

[1] based on MAC

A. Geometry

The aircraft configuration investigated was the XRF-1, a research configuration provided by Airbus and representative of a state of the art long range commercial transport aircraft [14]. The wind tunnel model geometry was used together with newly designed through flow nacelles and pylons[15] and additionally featured an empennage with horizontal and vertical tail planes. An illustration of the geometry is shown in Fig. 1. The wind tunnel model was equipped with a variety of sensors allowing to locally measure pressures on the surfaces of the aircraft. For a detailed description of available model instrumentation within the scope of this project the reader is referred to [22] and [15].

Special care was taken when setting up the simulation to accurately match the shape of the physical model tested in the wind tunnel under corresponding aerodynamic loads. This was achieved by applying the twist and bend distributions, measured on the wings during wind tunnel testing, using a mesh deformation technique. During wind tunnel testing the model was mounted on a sting protruding from the rear of the fuselage below the empennage. This sting was however removed from the model to simplify meshing and reduce simulation time. From previous studies it was known that the model support sting does influence the axial pressure gradient in the test section and that differences could be observed when using a simplified farfield approach in CFD [23] to reproduce wind tunnel results. However, in these studies this interference did not significantly alter the wing pressure distribution or the aerodynamic characteristics of the model [24] and therefore this simplification was not expected to influence the findings in this study.

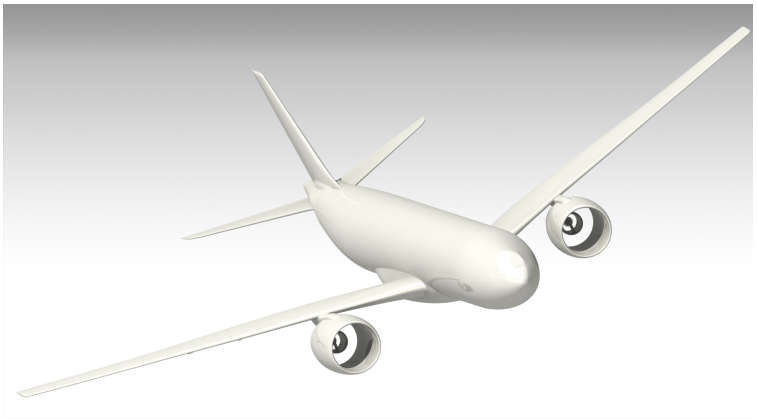

Fig. 1 XRF-1 wind tunnel model geometry with UHBR trough flow nacelles.

B. Mesh

The mesh for the hybrid RANS-LES simulation was an extension of a RANS mesh used extensively within the FOR 2895 for numerical simulations (hereafter denoted *base-mesh*) [12]. The *base-mesh* comprised of a hexahedra dominant boundary layer mesh and an unstructured tetrahedra volume mesh. Special care was taken to accurately resolve the boundary layer flow. Wall normal point distributions were adapted to ensure $y^+ < 0.4$ on the aircraft surfaces and a wall normal growth ratio of 1.12 was selected allowing for a fine resolution of the near wall velocity gradients. The total point count for the *base-mesh* of the aircraft half model summed up to 112 million points.

This *base-mesh* was modified in the region between pylon and fuselage to ensure a local resolution of a minimum of 10 cells per local boundary layer thickness in the LES region which is deemed the minimum requirement for the selected hybrid model [19]. To ensure this criteria was met in the entire region a precursor RANS simulation was run on the *base-mesh*. From this precursor simulation the mean local boundary layer thickness information was extracted at characteristic points as shown in Fig. 2a. The figure depicts a view on the inboard wing lower surface pressure distribution extracted from this precursor RANS simulation. A dominant shock occurring between 18 and 22% x/s can be seen. Furthermore, the extension of the resulting shock-induced flow separation between 20 and 30% y/s is shown by means of isolines of $C_{f,x} = 0$. Boundary layer thicknesses were extracted around the shock location complemented by additional extraction points further downstream almost up to the trailing edge. These reference points were then used to create a block structured mesh topology as shown in Fig. 2b. Each block was set up as a structured hexahedra block and it was ensured that the mesh resolution matched the minimum requirement of 10 cells per boundary layer thickness in both wall tangential coordinate directions. Thus, the local cell resolution in these directions is a function of the local boundary layer thickness. Small unstructured mesh blocks were built to connect the structured blocks while allowing to transition from finer to coarser mesh resolution when the local boundary layer thickness increases and thereby limiting the cell count. The height of the blocks in the LES region was defined as 1.5 times the maximum local boundary layer thickness of all reference points covered by the block. This criteria was satisfied up to $x/s \approx 0.25$. Downstream of this position, the wall-normal expansion of the separation became so large that it was decided to generate a block-structured mesh only in the area close to the wall and to fill the remaining volume of the separation region with tetrahedra (cf. Fig 7), which, however, still satisfy the local resolution criteria. The mesh blocks around the shock location were extended downstream by around 5% MAC to account for uncertainty and unsteady movement of the shock.

The final mesh was constructed from 797 million points with the vast majority of the points located in the LES region. The background mesh before refinement contained 112 million points. A large portion of the points in the LES region was located just upstream of the shock and close to the pylon in spanwise direction. Here the LES region was located close to the leading edge and therefore the local boundary layer thicknesses were very thin requiring a very fine local mesh resolution.

C. Hybrid RANS-LES Model

The method applied in study was based on the Improved Delayed Detached Eddy Simulation (IDDES) [25], which combines local RANS, DDES and wall-modeled LES functionalities (WMLES) in an automatic manner. It was further developed to be used in conjunction with Reynolds-stress based RANS models. A detailed description of the

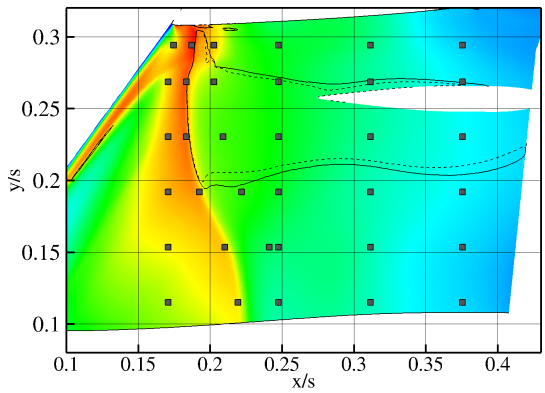

(a) Surface pressure contour and extraction points of local boundary layer thickness in preliminary RANS simulation

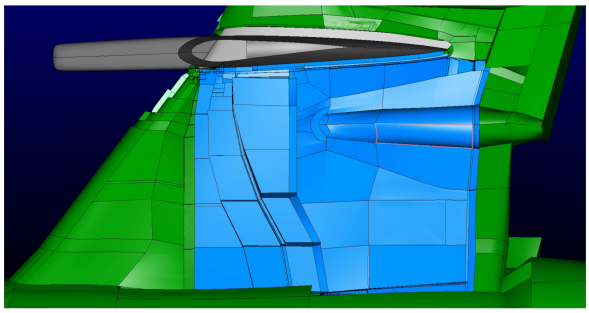

(b) Mesh block topology (green: RANS, blue: LES)

Fig. 2 Details of inboard wing lower surface mesh generation for IDDES.

modification required to apply the IDDES approach together with a Reynolds-stress background model can be found in [20]. Key element of the general IDDES method is the definition of a hybrid length scale l_{hyb} that serves to replace the integral length scale l_{RANS} of the underlying RANS-model.

$$l_{hyb} = \tilde{f}_d \left(1 + f_e\right) l_{\text{RANS}} + \left(1 - \tilde{f}_d\right) l_{\text{LES}} \tag{1}$$

Depending on the turbulent content of the inflow, the main blending function $\tilde{f}_d = \max\left\{\left(1 - f_{dt}\right), f_B\right\}$ can either switch to $1 - f_{dt}$ (DDES mode) or f_B (WMLES mode). The switching behavior is controlled by the delaying function f_{dt} which becomes close to 1 in areas with turbulent content and thus $\tilde{f}_d = f_B$. Otherwise $\tilde{f}_d$ reduces to $(1 - f_{dt})$ and also the elevating function f_e vanishes. The latter function f_e, which is only active in WMLES mode, is constructed to augment the modeled Reynolds stresses in RANS-LES intersection region and thus reducing the so-called log-layer mismatch.

Since the WMLES branch of IDDES is active in most of the relevant areas of the simulation, we describe this branch in more detail and refer to [25] for further details on the DDES branch. The WMLES blending function f_B is defined as:

$$f_B = \min\left\{2\exp(-9\alpha_g^2), 1.0\right\} \tag{2}$$

$$\alpha_g = 0.25 - \delta_w / h_{\max} \quad , \quad h_{\max} = \max\left\{\Delta x, \Delta y, \Delta z\right\} \tag{3}$$

with δ_w and Δi are defined as the wall distance and the local cell length in the respective coordinate direction. In contrast to f_{dt} the function f_B is solely grid dependent. Having this definition of f_B as well as a proper grid resolution, a maximum 5 % of the inner boundary layer are kept in RANS mode ($l_{hyb} = l_{RANS}$). In the remaining outer parts of the boundary layer l_{hyb} reduces to $l_{LES} = C_{DES}\Delta_{IDDES}$, with the IDDES filter function Δ_{IDDES}, which is a function of the local grid size, and the constant C_{DES}, which depends on the background RSM-RANS turbulence model and was selected as $C_{DES} = 0.65$ in this case. The above definition of the LES length scale l_{LES} leads to a Smagorinsky-type sub-grid model formulation for LES. As described in chapter II.B the grid was only refined locally in an area at the wing lower surface such that the resolution criteria for WMLES are fulfilled. In this way, the required computational resources, which are very large, could be reduced to a more manageable level. In order to avoid the IDDES mode to be active in regions away from the refined area, a local volume was defined in which the IDDES method is applied, while RANS mode is set outside this volume. An indication of this region is given in Fig. 3a. As can be seen it is confined to the area below the wing between the pylon and the fuselage. Parts of the pylon which are located close to the intersection of the pylon inboard surface and the wing lower surface are also located within this IDDES volume. This way the corner flow at the intersection of these surfaces can also be treated by the hybrid simulation approach.

We assume that it is necessary to resolve the outer part of boundary layers upstream of transonic shocks with LES in order to accurately simulate the dynamics of shock-boundary layer interaction. Therefore the WMLES mode of IDDES is required in the respective regions. One way to trigger WMLES locally is by injecting synthetic turbulence which was realized at the upstream edge of the IDDES box within the boundary layer of wing and pylon (cf. Fig.

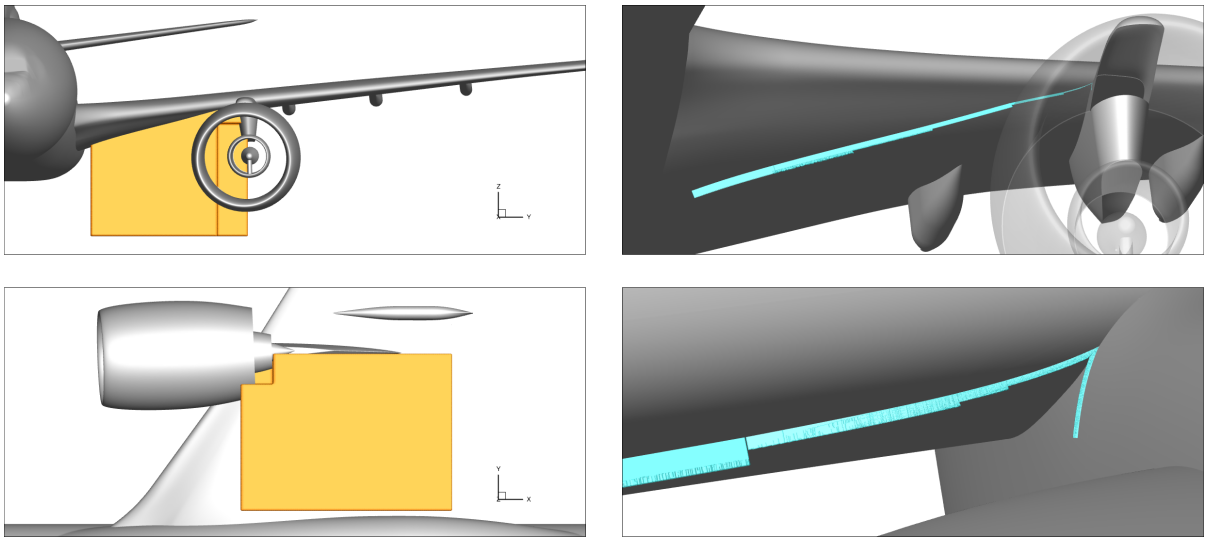

(a) IDDES box **(b) Synthetic turbulence generator**

Fig. 3 IDDES setup.

3b). A synthetic turbulence generator (STG) is further essential for a preferably seamless transition from RANS to WMLES mode in streamwise direction. Without synthetic turbulence, a "grey area" would emerge, referring to a zone of insufficiently resolved turbulence downstream of the RANS-WMLES interface. The STG applied in this study is based on [26] and [27] and generates local velocity fluctuations in space and time. The synthetic velocity fluctuations are calculated in such a way that their temporal statistics correspond to the RANS Reynolds stresses directly upstream of the RANS-WMLES interface. Thus, the modeled RANS turbulence is translated into temporally and spatially resolved turbulence. A recent extension of the implementation in TAU allows flexible placement of multiple STG fronts on 3D geometries via user-controlled polylines [28].

The wing sweep and the placement of the embedded WMLES region together with the highly three dimensional nature of the flow resulted in a large variation of local boundary layer thickness at the location of the STG. In fact, the expected local boundary layer thickness at the STG stretches over roughly two orders of magnitude from very thin boundary layers at the pylon-wing intersection where the STG lies close to the leading edge to very thick boundary layers at the wing root where the flow has already traveled some distance before reaching the STG. As the STG relies on a reference boundary layer thickness to generated representative velocity fluctuations it was not suitable to select one reference boundary layer thickness over the entire span. Therefore, the STG was split into 8 separate parts making use of the polyline implementation allowing for a step wise transition of the reference boundary layer thickness from the pylon to the wing root (cf. Fig. 3b).

D. Simulation

The hybrid IDDES method had been previously implemented into the unstructured cell-vertex based flow solver TAU [29]. The discretization of convective fluxes was done using a 2nd order central scheme with matrix dissipation relying on the Skew-symmetric central scheme by Kok [30] for the mean flow equations and using a first order Roe upwind scheme for the turbulence equations. A hybrid low-dissipation low-dispersion scheme [31] was applied to improve the accuracy of the model in the DES/LES regions while maintaining enough numerical dissipation to ensure stability of the simulation in the RANS region. The turbulence model applied in the RANS region was the SSG/LRR ln-ω Reynolds-stress model [32] relying on a simple gradient diffusion model [33] and an isotropic dissipation model. A dual time stepping scheme was applied along with a backward euler relaxation solver to move the simulation forward in time. The simulation was initialized from an unsteady RANS solution obtained on the LES grid with a fairly coarse time step. Time resolution for the hybrid simulation was then selected as 10000 time steps per convective time unit ($CTU = \frac{MAC}{U_\infty}$) which resulted in convective CFL numbers below unity in most of the cells in the LES region. This was a compromise between accuracy and computational resources because especially at the wing pylon junction close to the wing leading edge the local cell size in the LES domain turned out to be rather small and would have required an even

smaller time step. This would however led to a significant increase in computation time or a dramatic reduction in computed physical time steps. Cauchy convergence criteria were applied to ensure convergence of the inner iterations of the dual time stepping scheme and accelerate the simulation. The simulation was run for 4 CTU's before starting to gather data. This way it was ensured that the resolved turbulence had fully developed and that the remaining eddy viscosity stemming from the RANS model used during initialization was completely transported out of the LES region. The simulation was run for an additional 12 convective time units allowing detailed analysis of flow statistics.

E. Reference data

Experimental reference data was obtained from various wind tunnel tests conducted during the first research phase of the research initiative. The XRF-1 wind tunnel model (see Fig. 1) was tested within the ETW cryogenic wind tunnel facility. An overview of these test entries is given in [12]. Within the scope of this paper data from the second wind tunnel test *MK2* is used.

In the following chapters the validation of the numerical simulation relies mainly on steady and unsteady PSP measurements on the aircraft wings as well as data from surface pressure taps and several unsteady pressure transducers at various locations on the model. The unsteady PSP measurements thereby allow to assess time resolved surface pressure information on the entire wing surface. The method relies on a thin layer of special paint which changes its emitted luminescent intensity and lifetime under UV light depending on the local pressure. Using high speed cameras and sophisticated post processing this allowed to record time accurate pressures on the wing surface. For further reading on the PSP measurements applied the reader is referred to [16, 34–36].

III. Results

In the following results of the IDDES are shown and, where applicable, compared with wind tunnel results allowing to validate the suitability of this approach to model complex buffet phenomena on transport aircraft. Figure 4 gives a first impression of the simulation results. In Fig. 4a the mean pressure distribution on the wing lower surface is shown. Due to the presence of the nacelle and the low angle of attack a strong shock forms on the wing lower surface resulting in a shock induced separation. The latter is indicated by the region downstream of the shock that is encircled by the thin black line corresponding to $\mu_{C_{f,x}} = 0$ and therefore representing the mean shape of the flow separation. The separation encloses the first flap track fairing and extends up to the wing trailing edge. The spanwise extension of the shock induced separation ranges from approx. 18% span up to the pylon. The reader is reminded that these results are time averaged over 12 CTU and therefore do not represent that actual shape of the separation displayed in Fig. 4b. The position of the STG is indicated by the dashed line ranging from the pylon in inboard direction almost up to the wing root. To guide the reader through the following chapters four reference stations at constant span are established at 11.3, 15, 21.7 and 23.25% span as shown in Fig. 4a.

Figure 4b shows the unsteady nature and the resolution of the IDDES approach. Isosurfaces of Q-criterion at $Q = 10^9$ are shown colored by local Mach number. Very fine and thin structures can be observed just downstream of the STG which then get larger and larger when the flow separates from the wall due to the shock. Note that vortex structures outside the IDDES region are blanked to allow a clear visualization of the resolved turbulent flow. Otherwise the wake of the nacelle and core body would partly cover the LES area.

A. Synthetic Turbulence Generator

As already indicated in Chapter II, setting up such a simulation requires making a number of assumptions that are associated with corresponding uncertainties. The position of the STG has to be chosen carefully to ensure sufficient development of turbulent structures and dissipation of turbulent viscosity while minimizing the run-up length to limit the point count in the mesh. To investigate this, flow values were extracted at local reference positions as shown in Fig. 5. The reference slice position of $y/s = 0.23$ was chosen because at this spanwise position the shock is closest to the STG and therefore the turbulent structures have the shortest run-up length to develop before reaching the shock. As can be seen from Fig. 5 the SBLI occurs between 10 and 20 boundary layer thicknesses downstream of the STG. The reference boundary layer thickness taken for normalization was the local boundary layer thickness at the STG itself.

Figure 6 shows wall normal distributions of resolved and total turbulent kinetic energy at the aforementioned reference positions. Looking at the evolution of the total turbulent kinetic energy distribution over the run length shows the expected behavior that the turbulent kinetic energy and the profile thickness increase for further downstream positions. In addition a strong increase in total turbulent kinetic energy occurs at the location of the SBLI (10 to 20δ).

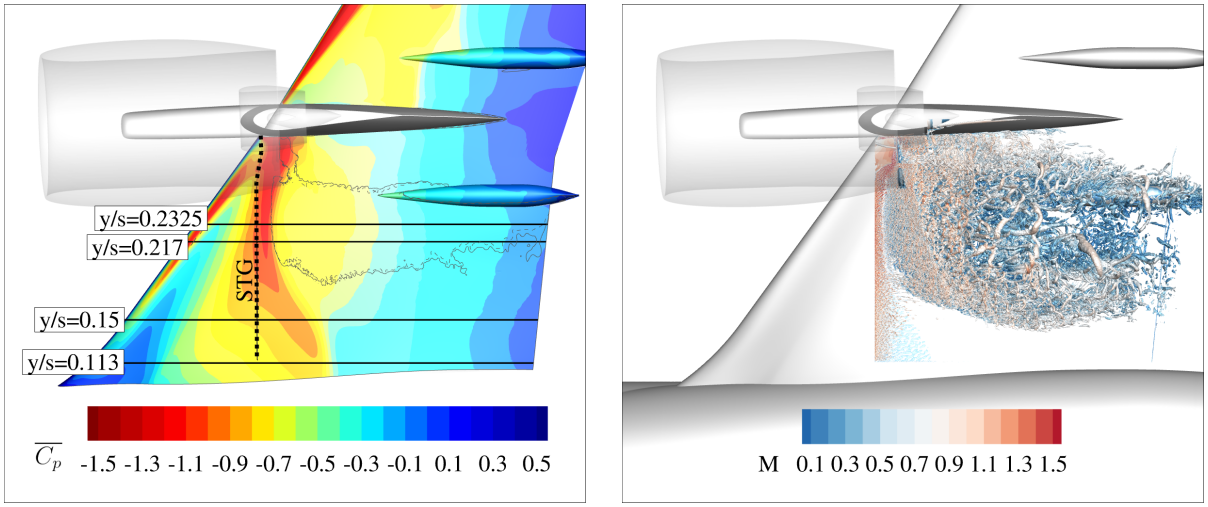

(a) Mean pressure coefficient **(b) Isosurface of Q-criterion colored by Mach number**

Fig. 4 Results of IDDES simulation on inboard wing lower surface.

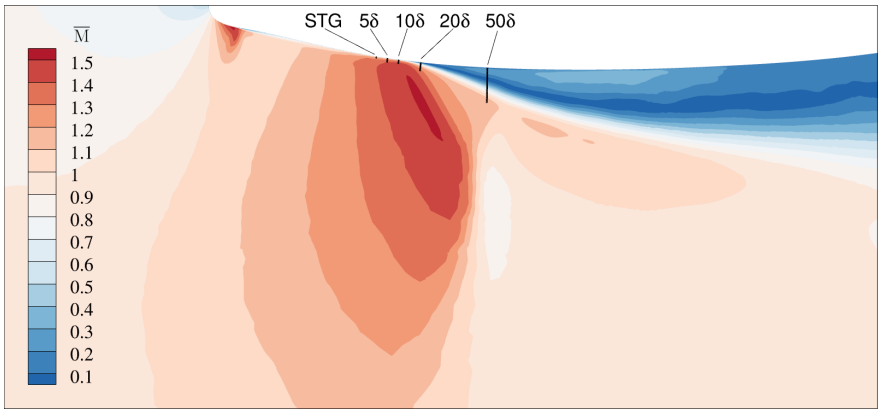

Fig. 5 Slice through flow field at $y/s = 0.23$ with mean Mach number contour.

The proportion of resolved turbulence is discussed below. At 5 δ downstream of the STG roughly half of the turbulent kinetic energy is already resolved by LES and this portion increases further for more downstream positions. At 10 δ the value of k_{ref} corresponds to 60% of k_{tot} at its maximum position at $\delta_w/\delta_{STG} \approx 0.07$ (cf. Fig 6a). To facilitate the visualization, the wall distance is shown on a logarithmic scale for positions further downstream in Fig. 6b. It is estimated that over 95% of the total turbulent kinetic energy are resolved for the 20 δ position where the flow starts to separate from the wall due to the adverse pressure gradient imposed by the shock. At 50 δ downstream of the STG where the flow has completely separated from the wall the portion of the resolved turbulent kinetic energy even surpasses 98%.

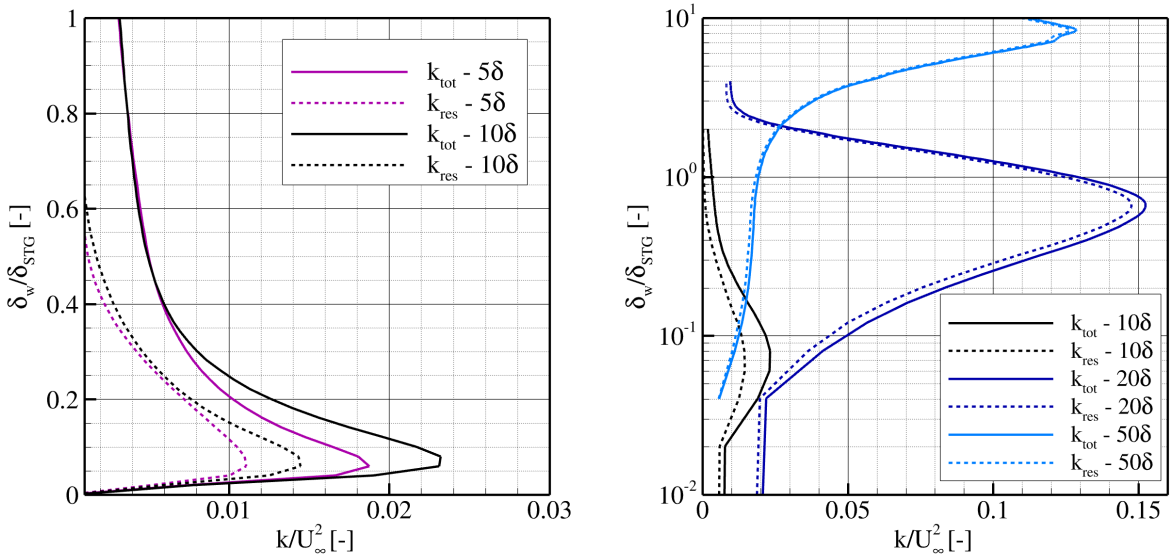

(a) STG vicinity **(b) Downstream evolution**

Fig. 6 Wall normal distributions of turbulent kinetic energy downstream of the STG at $y/s = 0.23$.

These findings give confidence that the STG was placed sufficiently upstream of the shock to allow the turbulent structures to develop sufficiently before the SBLI occurs. The fact that this investigated spanwise position exhibited the closest proximity between shock and STG allows this finding to be transferred to the entire LES area. It is noted that these findings are based on a mean shock location and that the distance between the STG and the shock front will be reduced during shock oscillation cycles for certain snapshots.

B. Hybrid Grid

When this simulation was set up, the mesh was constructed in way to account for certain shock movements which were estimated from observations gained during unsteady PSP measurements in the wind tunnel [18]. For the IDDES the SBLI location must not leave the refined mesh region when the shock is moving up and down around its mean location as the SBLI would then be modeled in RANS mode and not in LES mode and results would be erroneous.

To check this, the simulation was analyzed over its course of 16 CTU's and the extremes of the shock positions were evaluated. Figure 7 shows slices through the flow field at $y/s = 0.23$ for three different snapshots of the simulation representing extreme shock positions. During the transient phase of the simulation (first 4 CTU's), after switching to IDDES mode, the shock moved upstream and got close to the upstream border of the LES region, but never crossed the STG. This extreme position can be observed in Fig. 7a where the SBLI occurs just downstream of the STG and the resulting flow separation extends almost beyond the boundary of the first structured grid block downstream of the STG. During the averaging phase of the simulation (CTU 5 and beyond) the extreme shock positions were less pronounced. The most downstream position of the shock is shown in Fig. 7b with the shock hitting the boundary layer at the beginning of the second grid refinement block and the separated flow downstream falling well inside the refinement region. The most upstream shock position during the averaging phase is shown in Fig. 7c, again proving that the flow features of interest come to lie within the refinement blocks as expected.

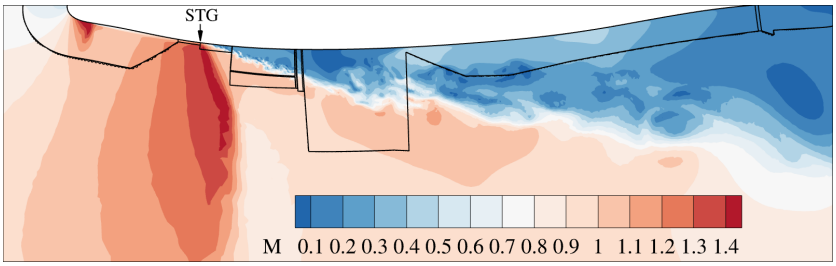

(a) Max. upstream position (transient phase)

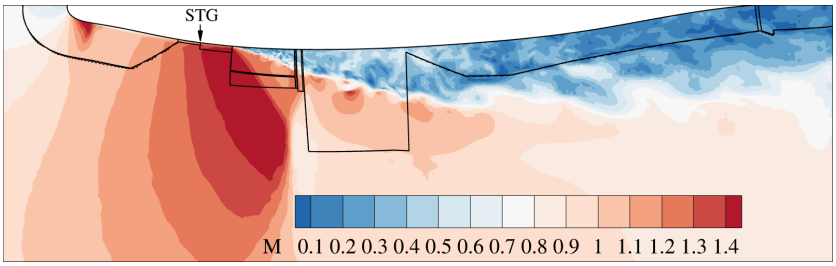

(b) Max. downstream position (averaging phase)

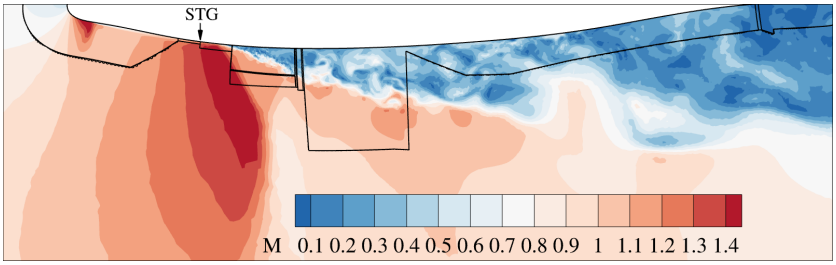

(c) Max upstream position (averaging phase)

Fig. 7 Slice through flow field and grid blocking at $y/s = 0.23$ with Mach number contour at maximum shock elongation positions.

C. Lower Surface Buffet

After confirming by the previous investigations that both the choice of the position of the STG and the extent of the grid refinement of the LES region were sufficient for analyzing the SBLI, an in-depth analysis of the lower wing buffet phenomenon was carried out.

1. Shock Position and Movement

A quantitative assessment of the results is given in Fig. 8. The temporal mean and standard deviation values of surface pressure were extracted at the four main spanwise positions shown in Fig. 4a. In addition to the IDDES results, data from simulations using a classic URANS approach are plotted for comparison. Note that the URANS simulation resulted in a steady state solution which is why it does not appear in the pressure variation plots in Fig. 8b. The data is compared against experimental wind tunnel data. At the station at $y/s = 0.2325$ the wind tunnel model was equipped with a full section of static pressure taps providing a dense distribution of pressure data. The mean pressure distribution for stations from $y/s = 0.113$ to 0.217 was extracted from PSP measurements on the wing lower surface giving continuous pressure information along the chord. The experimental reference data for the surface pressure variation was obtained from unsteady PSP measurements for all stations.

Note that the pressure distributions discussed in the following have to be interpreted in an inverse manner. Lower (negative) pressure coefficients are towards the top of the figures while higher (positive) pressure coefficients are oriented towards the bottom of the figure. Due to the low angle of attack the pressure coefficients on the wing lower surface are lower compared to the upper surface.

Looking at the main pressure distributions along the different spanwise stations in Fig. 8a it can be seen that the mean shock location moves from around 50% chord at the most inboard position to around 20% chord for $y/s = 0.2325$ which is in line with the pressure contour depicted in Fig. 4a. While both the URANS simulation as well as the IDDES reproduce this trend, only the IDDES accurately predicts the shock location in line with the wind tunnel experiment for all stations.

A more detailed analysis of section $y/s = 0.113$ shows that the curves of the pressure distribution of the URANS simulation and the IDDES match very well on both the upper and the lower surface, except for the shock location. In fact, the URANS curve is not visible in most of the diagram as it is covered by the IDDES curve. For this section the experimental data shows two dents in the pressure distribution at 30% and 40% chord respectively. Further analysis suggests that these deviations in pressure are related to surface imperfections on the wind tunnel model disturbing the optical measurements during PSP data acquisition.

The station at $y/s = 0.15$ shows a very similar behavior as just discussed. C_p curves of URANS and IDDES match very well on both upper and lower wing surface, except for the shock location where the curve of the IDDES is much closer to the experimental data. Deviations between the URANS curve and the IDDES curve also start to extend further downstream of the shock compared to the previous section. Although the agreement between the scale resolving simulation and the experiment is still excellent, a slight upstream shift of the shock location compared to the wind tunnel results can now be seen in the IDDES curve as well.

Proceeding further outboard to the spanwise position of $y/s = 0.217$ this trend is continued. Comparing the shock location of IDDES and the one obtained from PSP measurements a deviation is seen. The shock location in the URANS simulation is even closer to the experimental data in this case. However, in the region downstream of the shock, where the flow is completely separated as also indicated in Fig. 4a, only the IDDES is able to accurately reproduce the pressure distribution of the experiment.

The latter also holds true for the most outboard located section at $y/s = 0.2325$. In this case the pressure coefficients obtained from the pressure taps of the wind tunnel model come to lie precisely on the IDDES curve for both the upper and the lower wing surface. While the URANS simulation is again able to correctly reproduce the pressure distribution up to the shock, significant deviations are observed in the region of separated flow.

Considering the σ_{C_p} values in Fig. 8b the pressure variation at the shock location can be observed. Note that for the spanwise stations $y/s >= 0.15$ a dominant sharp peak in σ_{C_p} can be observed upstream of the shock location. These peaks correspond to the location of the STG. The most inboard section of $y/s = 0.113$ lies just outside of the IDDES region and is therefore not covered by the STG (cf. Fig. 4a). Interestingly it is this section where the pressure variation is predicted to be significantly higher compared to the experimental data obtained from unsteady PSP measurements. For all other sections the agreement in σ_{C_p} at the shock location between IDDES and unsteady PSP is excellent. Differences are observed downstream of the shock where the flow separation is present. In these regions the RMS values in the

IDDES are higher than what can be seen in the experimental data.

The unsteady PSP data provided in Fig. 8b exhibits certain secondary peaks apart from the main peak at the shock location for all investigated stations. The majority of these secondary peaks results from surface imperfections and they are not linked to any aerodynamic unsteadiness of the flow. After a detailed analysis we conclude that this applies to all secondary peaks at station $y/s = 0.113$, the peak at $x/c = 0.05$ at station $y/s = 0.15$, peaks at $x/c = 0.05$ and 0.17 as wells as alls peaks for $x/c > 0.85$ at station $y/s = 0.217$ and the peaks at $x/c = 0.05$ and $x/c > 0.85$ for station $y/s = 0.2325$.

The previously discussed findings are supported by the surface plots in Fig. 9. Here the mean and standard deviation of C_p are shown for the wing lower surface of the IDDES and the unsteady PSP measurements. Note that parts of the wing surface in the uPSP dataset are set to zero. On the one hand, there are the four flap track fairings and the pylon that were not covered with PSP coating, and on the other hand there, is the area of the wing that was not accessible due to the UHBR nacelle blocking the line of sight of the camera of the uPSP system.

The mean pressure distributions on the wing lower surface match well between both datasets (cf. Fig. 9a). Notable differences are observed at the outboard wing for $y/s > 0.7$ concerning the shock position and the trailing edge pressure. In the unsteady PSP data the shock is located significantly further downstream compared to the IDDES. Further analysis suggests that this is due to the RANS model being active in this area (cf. Fig. 3a) and its inability to model the strong SBLI correctly. In the midboard area of the wing, which is simulated using the RANS model as well, the shock imposes a weaker pressure gradient allowing the boundary layer to stay attached. This attached flow is accurately modeled by the RANS approach.

This is also supported by the plot of pressure variation in Fig. 9b. The outboard wing shows significant levels of σ_{C_p} in the unsteady PSP results, while the IDDES data only exhibits a small spot like increase in standard deviation at the leading edge at around 90% span. This supports the assumption that the RANS model applied leads to incorrect modeling of the physical phenomenon. Redirecting the readers attention to the LES region on the inboard wing, excellent agreement concerning the area of shock oscillation is observed. The s-shaped structure as well as the chordwise position match very well between IDDES and experiment. Differences are observed for the region of separated flow downstream of the shock where the experiment only shows moderate levels of pressure variation while the levels in the IDDES are more than twice as high. The reason for this deviation is currently not known, but it is assumed that it is linked to the limited number of snapshots available in the IDDES data and that increasing the simulation time of the scale resolving simulation would improve the consistency of the data.

2. Spectral Analysis

Three dimensional buffet effects are known to consist of broadband signals in the frequency domain [37–39]. Using Welch's method [40] PSD (power spectral density) spectra were extracted at the position of maximum $C_{p,RMS}$ (after filtering out the STG peak) for each spanwise section in Fig. 8. In order to reduce the influence of spatial noise present in the unsteady PSP measurements (cf. Fig. 9), data was averaged on a patch of 3x3 points around the target location before applying the PSD analysis. To non-dimensionalize the frequency content, the Strouhal number is computed with l_{ref} corresponding to the mean aerodynamic chord of the wind tunnel model as follows:

$$St = \frac{f \cdot l_{ref}}{U_\infty} \tag{4}$$

Results of this analysis are shown in Fig. 10. It becomes evident that the PSD analysis of the IDDES data results in low frequency resolution for lower Strouhal numbers. This is related to the limited time frame computed in the IDDES (12 CTU's with a sampling frequency of 27.47 MHz corresponding to 20 snapshots per CTU). For the uPSP data the frequency resolution is significantly higher, because the length of the time series recorded during wind tunnel testing is much longer (2500 CTU's with a sampling frequency of 2 kHz corresponding to around 1.5 snapshots per CTU) and therefore no symbols but only continous lines are plotted in Fig. 10. The sampling frequency of 2 kHz results in a maximal resolvable Strouhal number of 0.71 for the unsteady PSP data according to the Nyquist-Shannon criterion and therefore no data beyond that Strouhal number is shown for the uPSP curve.

Starting with the most inboard spanwise station of $y/s = 0.113$ the spectra of IDDES and uPSP agree very well. They show similar overall levels and the drop in PSD levels occurs at similar frequencies around $St \approx 0.4$. In addition the spectrum exhibits a bump in the Strouhal number range of 0.2 to 0.4 in both the simulation and the experiment. A similar statement can be made for the next section at $y/s = 0.15$ where the course of the spectra exhibit similar trends with the fall-off frequency again occurring around $St \approx 0.4$ whereby the IDDES curve is slightly shifted towards higher

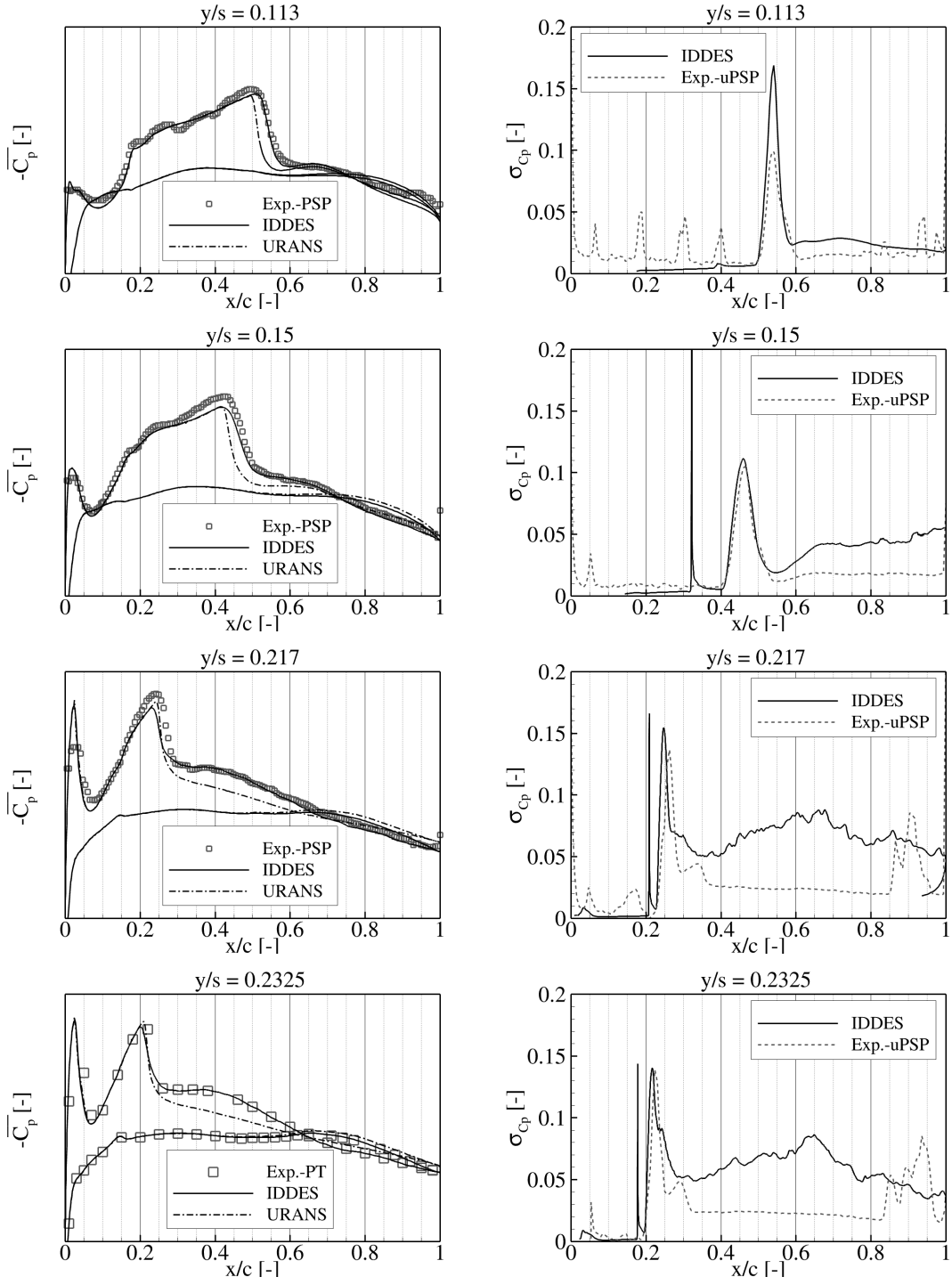

(a) Mean pressure distribution **(b) Surface pressure variation**

Fig. 8 Pressure distributions on inboard wing at various spanwise stations, comparison of experiment and simulation.

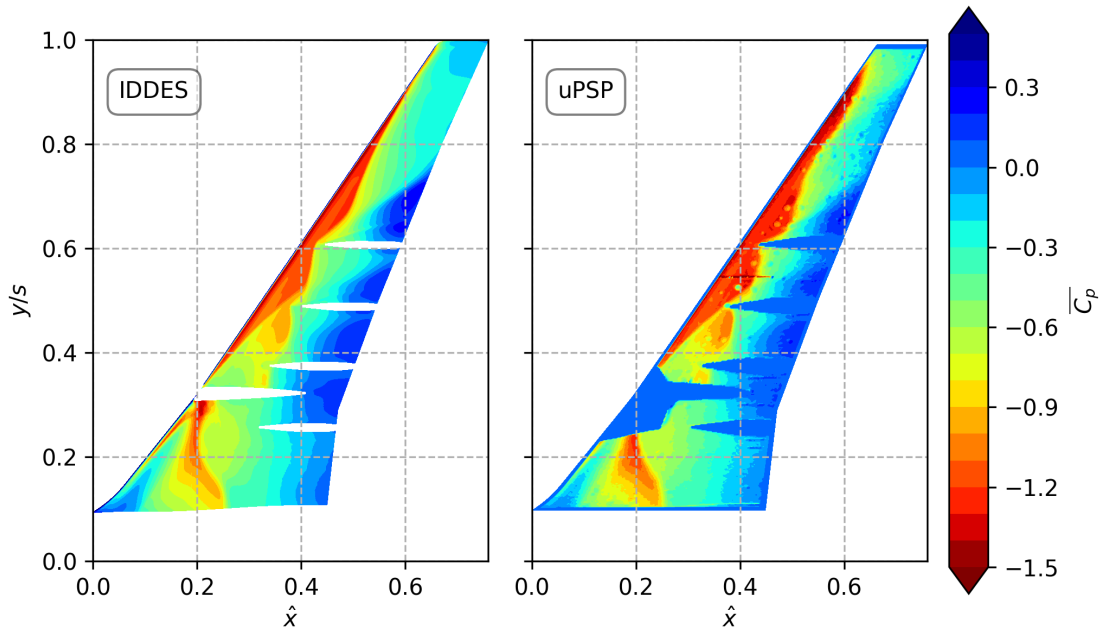

(a) Mean C_p

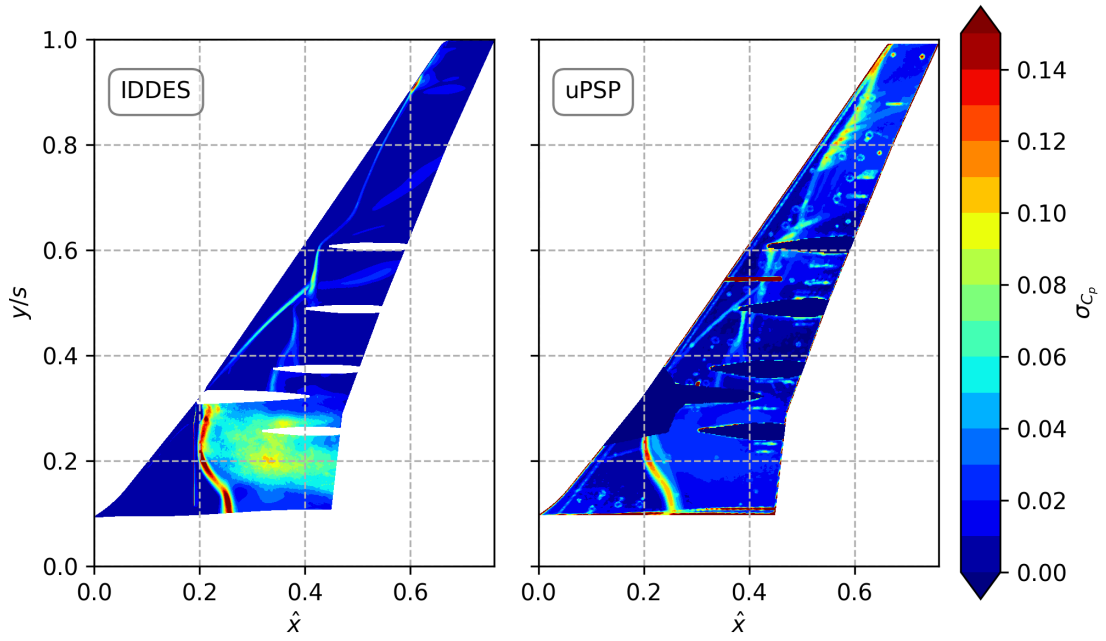

(b) Standard deviation of C_p

Fig. 9 Comparison of IDDES simulation and unsteady PSP measurements on the wing lower surface.

frequencies. Again a bump in the spectra can be observed at $St \approx 0.2 - 0.35$ for the uPSP data and at $St \approx 0.25 - 0.4$ for the IDDES curve. The latter also shows another peak at $St \approx 0.7$ that is not present in the PSP data. Further analysis suggests that this frequency range is associated with pressure fluctuations at the STG as indicated by the PSD curve computed at the location of the STG and added to the plot for sections 0.15 through 0.2325. Considering the section of $y/s = 0.217$ the agreement of the spectra is good but a significant increase in PSD levels can be seen for the IDDES curve in the Strouhal number range of 0.1 to 0.4. While an explanation for this deviation could not be found the strong drop in PSD levels at $St \approx 0.4$ still agrees very well in both the experimental as well as the numerical data. As for the previous station additional high frequency peaks can be seen in the spectrum of the IDDES at $St > 0.5$ that can be associated with the STG. For the most outboard section at $y/s = 0.2325$ the agreement between the spectrum extracted from IDDES and the spectrum extracted from uPSP is only fair. PSD levels do not agree precisely but at least show similar trends in the Strouhal number range of 0.15 to 0.5. An additional high frequency peak at $St \approx 0.6$ is present in the IDDES spectrum with the corresponding peak in STG spectrum occurring at $St \approx 0.9$.

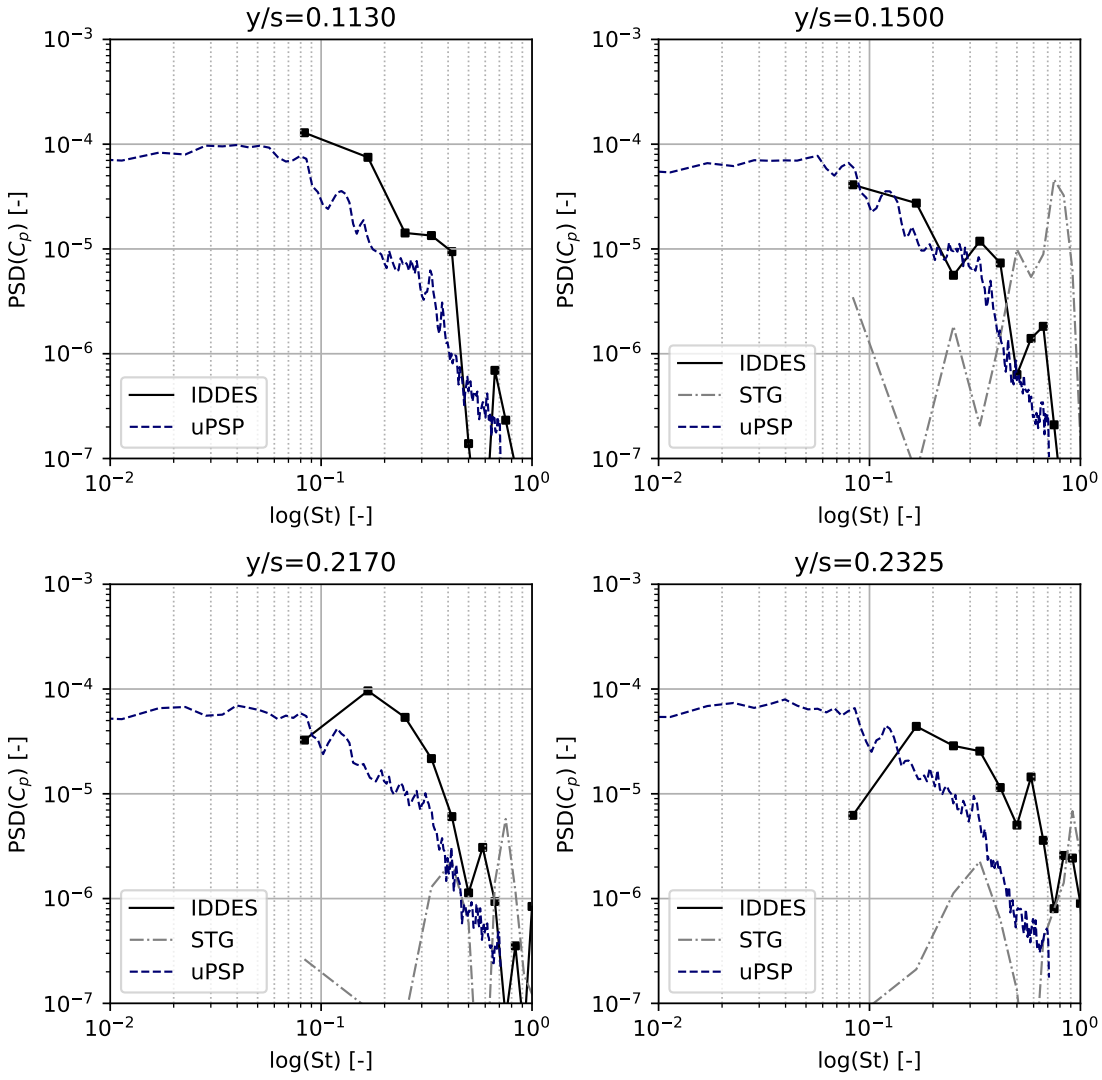

Fig. 10 PSD spectra at position of maximum $C_{p,rms}$ for various spanwise stations.

In summary the analysis therefore supports the previously presumed frequency range relevant for this lower wing buffet phenomenon [18] to occur at $St \approx 0.2 - 0.4$.

3. Corner Flow

The view on the wing lower surface close to the pylon was blocked by the nacelle during wing tunnel testing (cf. Fig. 9), therefore no unsteady PSP data was recorded in this area. To validate the results of the IDDES in this region we rely on data from 6 unsteady pressure transducers located on the pylon at the inboard wing-pylon intersection as shown in. Fig. 11a. The unsteady pressure data of these sensors was recorded on the same run as the unsteady PSP measurements discussed before, resulting in a time series of 2500 CTU's with a sampling frequency of 10 kHz and 7.3 samples per CTU.

In Fig. 11a the mean pressure coefficients together with an error bar of one standard deviation are shown for the IDDES and the pressure transducers from the wind tunnel experiment. The mean pressure coefficients in the wing-pylon junction agree very well showing also similar values in standard deviation. The maximum variation in the pressure is observed at sensor positions 2 through 4 (numbered front to back) corresponding to the mean shock location.

An analysis of the frequency content is done again by using Welch's method extracting PSD spectra at sensors location 2 and 4. These locations were selected because the IDDES exhibits the strongest pressure fluctuations at location 2 and the wind tunnel experiment at location 4. The results are shown in Fig. 11b. The agreement between simulation and experiment at position 2 is good except for a distinct peak around $St = 0.4$ in the IDDES that is not present in the experiment. Considering position 4 the agreement between experiment and IDDES is very poor with the PSD levels of the simulation being significantly lower compared to the experiment over the entire frequency range. The analysis at position 4 also exhibits the distinct peak at $St = 0.4$ similar to position 2. The deficiency in the spectra of the junction flow may be related to violating the $CFL_{conv} < 1$ constraint in the IDDES due to practical reasons (see Chapter II.D). In addition this area is influenced by the nacelle wake flow. The turbulence of the nacelle wake and the upstream boundary layer on the nacelle was however not resolved in LES mode but in RANS mode posing another possible explanation why such a large deviation is observed.

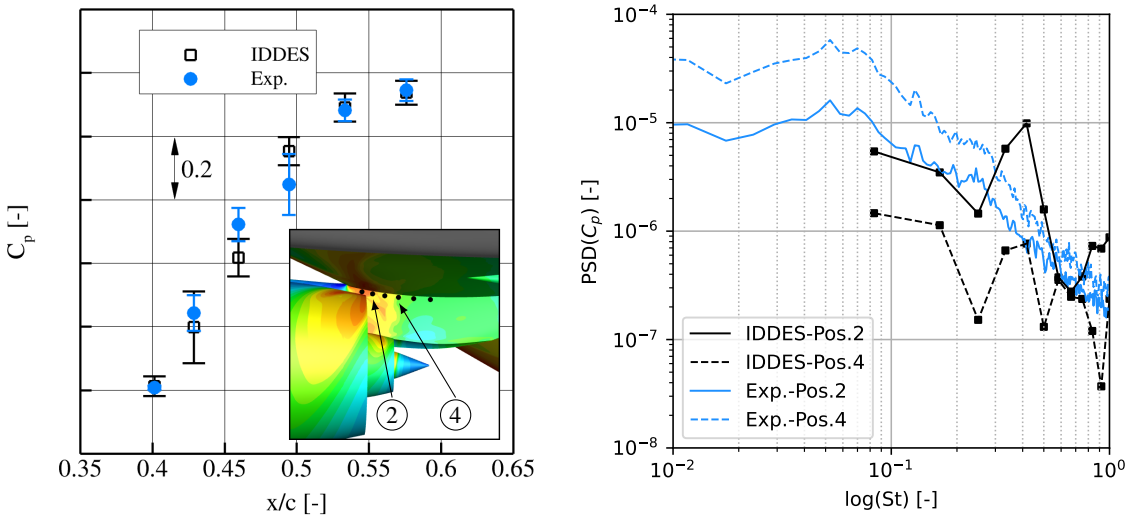

(a) Corner flow pressure coefficients **(b) PSD spectra of sensors 2 and 4**

Fig. 11 Pressure distributions on pylon at wing-pylon intersection, comparison of experiment and simulation.

IV. Conclusion

A novel hybrid RANS-LES simulation setup based on the IDDES approach coupled with a Reynolds-stress background model was applied to a complex shock boundary layer interaction phenomenon on a state of the art transport aircraft configuration. The application of IDDES together with synthetic turbulence injection allowed to assess the lower wing buffet effect due to the installation of the UHBR nacelle with a remarkable level of detail. Considering the simulation setup it was found that a distance of 10-20 boundary layer thicknesses between STG and mean shock location is sufficient for enough resolved turbulence to develop and for the remaining eddy viscosity to be dissipated.

Assumptions considering the required mesh resolution in the LES region were found to be transferable from previous studies and match current best practices observed within the LES community of at least 10 cells per local boundary layer thickness.

The application of the IDDES approach allowed it to model the pressure distribution at and around the mean shock location in the LES region with high precision. Excellent agreement with experimental data was observed that was not possible with RANS based simulation. In addition the IDDES reproduced the position as well as the levels of surface pressure variation at the shock due to the unsteady shock movements with remarkable accuracy. An analysis of the spectral content yielded good agreement between IDDES and unsteady PSP measurements concerning the surface pressure variations at the shock. The comparison was however limited in terms of frequency resolution in the low Strouhal number domain due the limited number of snapshots available with the hybrid simulation. Nevertheless, the simulation data suggested that the lower wing buffet phenomenon is associated with frequencies in the Strouhal number range of $St = 0.2$ to 0.4 which is in line with previous studies based on pure experimental data.

While the computational resources required for this study were certainly significant, we have shown that the application of a highly-resolved local wall-modelled LES based on hybrid RANS-LES is in principle feasible, but also beneficial for flow predictions of complex transport aircraft configurations if the problem of interest is carefully chosen. For an extension to flow conditions addressing higher Reynolds numbers further developments are necessary to increase efficiency and applicability of the method. Further improvements of the results, especially for the standard deviation of pressure in the region of strongly separated flow as well as the low frequency domain of the spectral analysis, are expected for longer simulated physical time series. Further decreasing the physical time step and strictly adhering to the $CFL_{conv} \leq 1$ condition are expected to improve results in the wing pylon intersection regions as well as including the nacelle wake in the LES region.

Appendix

A. Spatial averaging of uPSP data

Unsteady PSP data was averaged on a 3x3 patch before applying the Welch's method to reduce the impact of spatial noise present in the data. A study has been conducted to ensure that this averaging does not alter the spectra in the suspected buffet frequency range (St=0.2-0.4). The results in Fig. 12 show that when applying an averaging on a 3x3 point patch only high frequency contents for Strouhal numbers above 0.4 are affected. When averaging over a larger number of points before the PSD analysis this reduction in high frequency content is still observed and in addition overall PSD levels are being reduced without significantly altering the shape of the spectrum.

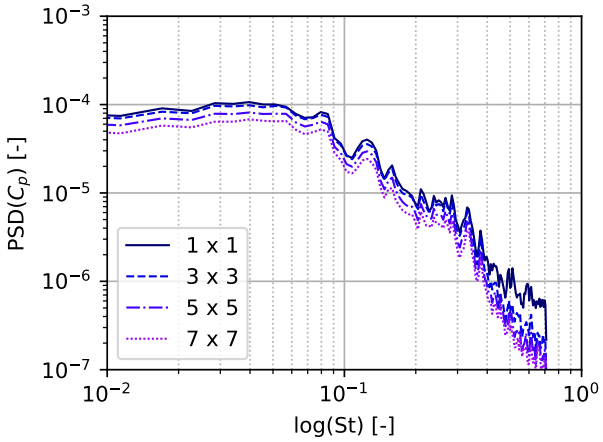

Fig. 12 Influence of averaging patch size on PSD spectra in uPSP data.

V. Acknowledgement

The authors gratefully acknowledge the Deutsche Forschungsgemeinschaft DFG (German Research Foundation) for funding this work in the framework of the research unit FOR 2895. The authors would like to thank the Helmholtz Gemeinschaft HGF (Helmholtz Association), Deutsches Zentrum für Luft- und Raumfahrt DLR (German Aerospace Center) and Airbus for providing the wind tunnel model and financing the wind tunnel measurements as well as public support to mature the test methods applied by DLR and ETW.

References

[1] C.-C. Rossow, H. H. V. S., J.-L. Godard, "Investigation of Propulsion Integration Interference Effects on a Transport Aircraft Configuration," *Journal of Aircraft*, Vol. 31, No. 5, 1994, pp. 1022–1030. https://doi.org/10.2514/3.46605.

[2] Rudnik, R., Rossow, C.-C., and v. Geyr, H. F., "Numerical simulation of engine/airframe integration for high-bypass engines," *Aerospace Science and Technology*, Vol. 6, No. 1, 2002, pp. 31–42. https://doi.org/10.1016/s1270-9638(01)01139-7.

[3] David L. Daggett, R. T. K., Stephen T. Brown, "Ultra-Efficient Engine Diameter Study," techreport 2003-212309, NASA, 2003.

[4] Stankowski, T. P., MacManus, D. G., Robinson, M., and Sheaf, C. T., "Aerodynamic Effects of Propulsion Integration for High Bypass Ratio Engines," *Journal of Aircraft*, Vol. 54, No. 6, 2017, pp. 2270–2284. https://doi.org/10.2514/1.c034150.

[5] Lange, F., "Aerodynamic Optimization of an UHBR Engine Position on a Short Range Aircraft Configuration at Cruise Flight Conditions," *2018 Applied Aerodynamics Conference*, American Institute of Aeronautics and Astronautics, 2018. https://doi.org/10.2514/6.2018-3811.

[6] Magrini, A., Buosi, D., and Benini, E., "Analysis of installation aerodynamics and comparison of optimised configuration of an ultra-high bypass ratio turbofan nacelle," *Aerospace Science and Technology*, Vol. 128, 2022.

[7] Magrini, A., Benini, E., Yao, H.-D., Postma, J., and Sheaf, C., "A review of installation effects of ultra-high bypass ratio engines," *Progress in Aerospace Sciences*, Vol. 119, 2020, p. 100680. https://doi.org/10.1016/j.paerosci.2020.100680.

[8] Apetrei, R. M., Ciobaca, V., Curiel-Sosa, J. L., and Qin, N., "Unsteady shock front waviness in shock-buffet of transonic aircraft," *Advances in Aerodynamics*, Vol. 2, No. 1, 2020. https://doi.org/10.1186/s42774-020-00034-x.

[9] Ehrle, M., Waldmann, A., Lutz, T., and Krämer, E., "Simulation of transonic buffet with an automated zonal DES approach," *CEAS Aeronautical Journal*, Vol. 11, No. 4, 2020, pp. 1025–1036. https://doi.org/10.1007/s13272-020-00466-7.

[10] Ohmichi, Y., Ishida, T., and Hashimoto, A., "Modal Decomposition Analysis of Three-Dimensional Transonic Buffet Phenomenon on a Swept Wing," *AIAA Journal*, Vol. 56, No. 10, 2018, pp. 3938–3950. https://doi.org/10.2514/1.j056855.

[11] Sartor, F., and Timme, S., "Delayed Detached–Eddy Simulation of Shock Buffet on Half Wing–Body Configuration," *AIAA Journal*, Vol. 55, No. 4, 2017, pp. 1230–1240. https://doi.org/10.2514/1.j055186.

[12] Lutz, T., Kleinert, J., Waldmann, A., Koop, L., Yorita, D., Dietz, G., and Schulz, M., "Research Initiative for Numerical and Experimental Studies on High-Speed Stall of Civil Aircraft," *Journal of Aircraft*, Vol. 60, No. 3, 2023.

[13] Hartzuiker, J., "The european transonic wind-tunnel ETW: A cryogenic solution," *The Aeronautical Journal*, Vol. 88, No. 879, 1984, pp. 379–394.

[14] Mann, A., Thompson, G., and White, P., "Civil Aircraft Wind Tunnel Feature Rich Testing at the Edge of the Envelope," *54th 3AF International Conference on Applied Aerodynamics*, 3AF, Paris-France, 2019.

[15] Spinner, S., and Rudnik, R., "Design of a UHBR Through Flow Nacelle for High Speed Stall Wind Tunnel Investigations," *Deutscher Luft- und Raumfahrt Kongress 2021*, Deutsche Gesellschaft für Luft- und Raumfahrt - Lilienthal-Oberth e.V., 2021. https://doi.org/10.25967/550043.

[16] Yorita, D., Henne, U., and Klein, C., "Time-resolved Pressure Sensitive Paint Measurements for Cryogenic Wind Tunnel Tests," *CEAS Aeronautical Journal*, Vol. 15, 2024, pp. 37–47.

[17] Bosbach, J., Konrath, R., Geisler, R., Philipp, F., Agocs, J., Koop, L., and Kühn, C., "Capturing Unsteady Flow Phenomena at High Speed Stall Conditions by Adaptation and Application of Cryogenic PIV," *AIAA SCITECH 2024 Forum*, American Institute of Aeronautics and Astronautics, 2024. https://doi.org/10.2514/6.2024-2665.

[18] Spinner, S., and Rudnik, R., "Experimental assessment of wing lower surface buffet effects induced by the installation of a UHBR nacelle," *CEAS Aeronautical Journal*, Vol. 15, 2024, pp. 49–59. https://doi.org/10.1007/s13272-022-00632-z.

[19] Herr, M., Probst, A., and Radespiel, R., "Grey area in embedded wall-modelled LES on a transonic nacelle-aircraft configuration," *CEAS Aeronautical Journal*, Vol. 15, 2024, pp. 5–22. https://doi.org/10.1007/s13272-023-00664-z.

[20] Herr, M., Radespiel, R., and Probst, A., "Improved Delayed Detached Eddy Simulation with Reynolds-stress background modelling," *Computers & Fluids*, Vol. 265, 2023, p. 106014. https://doi.org/10.1016/j.compfluid.2023.106014.

[21] Federal Aviation Administration, D. o. T., "14 CFR 25.335 Design airspeeds," , 2023. URL https://www.govinfo.gov/content/pkg/CFR-2023-title14-vol1/pdf/CFR-2023-title14-vol1-sec25-335.pdf.

[22] Waldmann, A., Ehrle, M., Kleinert, J., Yorita, D., and Lutz, T., "Mach and Reynolds number effects on transonic buffet on the XRF-1 transport aircraft wing at flight Reynolds number," *Experiments in Fluids*, Vol. 64, No. 102, 2023.

[23] Heidebrecht, A., "Simulating Wind Tunnels: CFD models for a transonic slotted test section," *4th Symposium on Integrating CFD and Experiments in Aerodynamics*, 2009.

[24] Heidebrecht, A., "Simulation and Model Support Correction for Slotted Wall Transonic Wind Tunnels," *47th Applied Aerodynamics Symposium*, 2012.

[25] Shur, M. L., Spalart, P. R., Strelets, M. K., and Travin, A. K., "A hybrid RANS-LES approach with delayed-DES and wall-modelled LES capabilities," *International Journal of Heat and Fluid Flow*, Vol. 29, No. 6, 2008, pp. 1638–1649. https://doi.org/10.1016/j.ijheatfluidflow.2008.07.001.

[26] Adamian, D., and Travin, A., "An Efficient Generator for Synthetic Turbulence at RANS-LES Interface in Embedded LES of Wall-Bounded and Free Shear Flow," *Computational Fluid Dynamics 2010*, edited by A. Kuzmin, Springer Berlin Heidelberg, St. Petersburd, Russia, 2011. https://doi.org/10.1007/978-3-642-17884-9.

[27] Francois, D. G., Radespiel, R., and Probst, A., "Forced Synthetic Turbulence Approach to Stimulate Resolved Turbulence Generation in Embedded LES," *Progress in Hybrid RANS-LES Modelling*, Springer International Publishing, 2015, pp. 81–92. https://doi.org/10.1007/978-3-319-15141-0_6.

[28] Probst, A., Soliman, E., Probst, S., Orlt, M., and Knopp, T., "Towards efficient hybrid RANS-LES for industrial aeronautical applications," *14th International ERCOFTAC Symposium on Engineering Turbulence Modeling and Measurements 2023*, 2023.

[29] Gerhold, T., "Overview of the Hybrid RANS Code TAU," *MEGAFLOW - Numerical Flow Simulation for Aircraft Design*, edited by N. Kroll and J. K. Fassbender, Springer Berlin Heidelberg, Berlin, Heidelberg, 2005, pp. 81–92.

[30] Kok, J., "A high-order low-dispersion symmetry-preserving finite-volume method for compressible flow on curvilinear grids," *Journal of Computational Physics*, Vol. 228, 2009, pp. 6811–6832.

[31] Probst, A., Löwe, J., Reuß, S., Knopp, T., and Kessler, R., "Scale-Resolving Simulations with a Low-Dissipation Low-Dispersion Second-Order Scheme for Unstructured Flow Solvers," *AIAA Journal*, Vol. 54, No. 10, 2016, pp. 2972–2987. https://doi.org/10.2514/1.j054957.

[32] Eisfeld, B., and Rumsey, C., "Length-Scale Correction for Reynolds-Stress Modeling," *AIAA Journal*, Vol. 58, No. 4, 2020, pp. 1518–1528. https://doi.org/https://doi.org/10.2514/1.J058858.

[33] Eisfeld, B., "Implementation of Reynolds Stress Models into the DLR-FLOWer Code," techreport DLR-IB 124-2004/31, Institute of Aerodynamics anf Flow Technologies, DLR, 2004.

[34] Yorita, D., Klein, C., Henne, U., Ondruss, V., Beifuss, U., Hensch, A.-K., Guntermann, P., and Quest, J., "Investigation of a Pressure Sensitive Paint Technique for ETW (Invited)," *55th AIAA Aerospace Sciences Meeting*, American Institute of Aeronautics and Astronautics, 2017. https://doi.org/10.2514/6.2017-0335.

[35] Yorita, D., Klein, C., Henne, U., Ondrus, V., Beifuss, U., Hensch, A.-K., Longo, R., Guntermann, P., and Quest, J., "Successful Application of Cryogenic Pressure Sensitive Paint Technique at ETW," *2018 AIAA Aerospace Sciences Meeting*, American Institute of Aeronautics and Astronautics, 2018. https://doi.org/10.2514/6.2018-1136.

[36] Klein, C., Yorita, D., Henne, U., Kleindienst, T., Koch, S., and Ondrus, V., "Unsteady pressure measurements by means of PSP in cryogenic conditions," *AIAA Scitech 2020 Forum*, American Institute of Aeronautics and Astronautics, 2020. https://doi.org/10.2514/6.2020-0122.

[37] Roos, F., "The buffeting pressure field of a high-aspect-ratio swept wing," *18th Fluid Dynamics and Plasmadynamics and Lasers Conference*, American Institute of Aeronautics and Astronautics, 1985. https://doi.org/10.2514/6.1985-1609.

[38] Dandois, J., "Experimental study of transonic buffet phenomenon on a 3D swept wing," *Physics of Fluids*, Vol. 28, No. 1, 2016, p. 016101. https://doi.org/10.1063/1.4937426.

[39] Steimle, P. C., Karhoff, D.-C., and Schröder, W., "Unsteady Transonic Flow over a Transport-Type Swept Wing," *AIAA Journal*, Vol. 50, No. 2, 2012, pp. 399–415. https://doi.org/10.2514/1.j051187.

[40] Welch, P., "The use of the fast Fourier transform for the estimation of power spectra: A method based on time averaging over short, modified periodograms," *IEEE Transactions on Audio and Electroacoustics*, Vol. 15, No. 2, 1967, pp. 70–73. https://doi.org/10.1109/TAU.1967.1161901.